Indo-Pacific Climate Interactions in the Absence of an Indonesian Throughflow

Jules B. Kajtar, Agus Santoso, and Matthew H. England

ARC Centre of Excellence for Climate System Science, and Climate Change Research Centre, University of New South Wales, Sydney, New South Wales, Australia

Wenju Cai

CSIRO Marine and Atmospheric Research, Aspendale, Victoria, Australia

ABSTRACT

The Pacific and Indian Oceans are connected by an oceanic passage called the Indonesian Throughflow (ITF). In this setting, modes of climate variability over the two oceanic basins interact. El Niño–Southern Oscillation (ENSO) events generate sea surface temperature anomalies (SSTAs) over the Indian Ocean that, in turn, influence ENSO evolution. This raises the question as to whether Indo-Pacific feedback interactions would still occur in a climate system without an Indonesian Throughflow. This issue is investigated here for the first time using a coupled climate model with a blocked Indonesian gateway and a series of partially decoupled experiments in which air–sea interactions over each ocean basin are in turn suppressed. Closing the Indonesian Throughflow significantly alters the mean climate state over the Pacific and Indian Oceans. The Pacific Ocean retains an ENSO-like variability, but it is shifted eastward. In contrast, the Indian Ocean dipole and the Indian Ocean basinwide mode both collapse into a single dominant and drastically transformed mode. While the relationship between ENSO and the altered Indian Ocean mode is weaker than that when the ITF is open, the decoupled experiments reveal a damping effect exerted between the two modes. Despite the weaker Indian Ocean SSTAs and the increased distance between these and the core of ENSO SSTAs, the interbasin interactions remain. This suggests that the atmospheric bridge is a robust element of the Indo-Pacific climate system, linking the Indian and Pacific Oceans even in the absence of an Indonesian Throughflow.

1. Introduction

The El Niño–Southern Oscillation (ENSO) is the dominant global climate mode on interannual time scales, exerting profound impacts upon the environment and economies worldwide. Originating in the equatorial Pacific Ocean, ENSO impacts air–sea processes over remote oceans (Klein et al. 1999; Lau and Nath 2003; Liu and Alexander 2007; Du et al. 2009), generating anomalous sea surface temperature anomalies (SSTAs). These remote SSTAs can, in turn, feed back onto ENSO variability in the Pacific. A particularly strong feedback is exerted by the Indian Ocean [see Santoso et al. (2012)

and references therein], to which the Pacific Ocean is directly connected via the Indonesian Throughflow.

During their growth phase, El Niño and La Niña events occasionally induce positive and negative Indian Ocean dipole (IOD) events, respectively, which peak in boreal autumn (Saji et al. 1999). The IOD is a coupled mode of variability, involving a seesaw pattern in SSTAs in the western and eastern tropical Indian Ocean. A positive phase of the IOD corresponds with anomalously cool SST in its eastern pole and anomalously warm SST in the western pole (vice versa for the negative phase). As El Niño and La Niña events peak in boreal winter, they tend to induce basinwide warming and cooling, respectively, over the tropical Indian Ocean, which is commonly referred to as the Indian Ocean basinwide mode (IOBM; Klein et al. 1999; Lau and Nath 2003; Du et al. 2009). These Indian Ocean modes of variability in turn feed back onto ENSO processes in the Pacific, influencing its period, amplitude, and thus its

predictability (e.g., Kug and Kang 2006; Luo et al. 2010; Izumo et al. 2010; Santoso et al. 2012).

It has long been believed that the primary way in which Indian Ocean climate modes feed back onto ENSO is via their influence on the atmospheric Walker circulation (Lau and Nath 2000, 2003; Alexander et al. 2002; Wu and Kirtman 2004; Annamalai et al. 2005; Behera et al. 2006; Potemra and Schneider 2007a). This can be inferred, for instance, by suppressing air–sea interactions over the Indian Ocean in climate models (e.g., Wu and Kirtman 2004; Behera et al. 2006; Dommenget et al. 2006; Santoso et al. 2012). Warm IOBM has been found to drive easterly wind anomalies over the western Pacific that act to dampen El Niño events (Santoso et al. 2012) and accelerate the transition to a La Niña event (Kug and Kang 2006; Kug et al. 2006). These easterly wind anomalies induce eastward propagating upwelling Kelvin waves along the equatorial Pacific that eventually terminate the El Niño event (Wang et al. 1999). The IOD has also been thought to influence ENSO dynamical processes in the Pacific through the atmospheric bridge, via an alteration of the Walker circulation (Izumo et al. 2010, 2014). During a negative IOD for instance, which tends to co-occur with a developing La Niña, the anomalously warm eastern Indian Ocean induces easterly wind anomalies that deepen the thermocline over the western Pacific warm pool. The eastward propagating upwelling Kelvin waves reinforce the shallowing thermocline in the eastern Pacific, thus enhancing development of the ensuing La Niña. The abrupt termination of these wind anomalies at the end of the negative IOD event in November allows the anomalous warming to spread toward the eastern Pacific, preconditioning for an El Niño in the following year (Izumo et al. 2010).

The atmospheric bridge is thus an important element of the Indo-Pacific climate system. However, its role in coupling the two basins is likely to be complicated by the presence of the Indonesian Throughflow (ITF). Yuan et al. (2011, 2013) argued that the ocean channel mechanism is more important than the atmospheric bridge in the coupling between ENSO and the IOD at longer time lags. With both models and observations, they showed that IOD events can generate upwelling anomalies in the eastern tropical Indian Ocean, inducing Kelvin waves that propagate through the Indonesian seas to the equatorial Pacific Ocean.

The idea of a dominant ocean channel mechanism seems reasonable given that the ITF transports a significant volume of water and heat from the Pacific to Indian Ocean. On average, the flow rate is 10–15 Sv (1 Sv $\equiv$ $10^6 \, \text{m}^3 \, \text{s}^{-1}$; Potemra 1999; Gordon 2005; Wijffels et al. 2008), and the heat transport is on the order of 0.5–1.0 PW (Vranes et al. 2002; England and Huang 2005). In addition, the ITF exhibits significant interannual variability (e.g., Meyers 1996; England and Huang 2005; van Sebille et al. 2014) controlled by pressure differences between the western Pacific and eastern Indian Ocean, which are in turn linked to ENSO and Indian Ocean variability. The ITF can also be directly influenced by changes in oceanic circulation induced by both ENSO and the IOD (e.g., England and Huang 2005; Potemra and Schneider 2007b; Sprintall et al. 2009; Sprintall and Révelard 2014).

Blocking the Indonesian Throughflow in coupled climate models significantly alters the global climate and ENSO (Schneider 1998; Wajsowicz and Schneider 2001; Song et al. 2007; Santoso et al. 2011). For instance, blocking the ITF results in weaker trade winds, flatter equatorial thermocline, and weaker upwelling across the Pacific Ocean, leading to an alteration of ENSO characteristics. This demonstrates that the ITF is an important component of the Indo-Pacific climate system. Thus, it is illuminating to assess the significance of the atmospheric bridge mechanism in light of the prominent presence of the ITF. An understanding of the role of the two available pathways may help to improve ENSO, IOD, and IOBM forecasting, and it can shed light on Indo-Pacific feedback interactions throughout Earth's history, over which the ITF has varied substantially (e.g., Cane and Molnar 2001; Kuhnt et al. 2004).

One way to evaluate the role of the atmospheric bridge is to utilize a climate model with a closed ITF and conduct partially decoupled experiments in which the air–sea interactions are suppressed over each oceanic basin independently. Each of the two experimental elements—that is, a closed ITF and suppressed air–sea interactions—has been analyzed separately in previous studies (Santoso et al. 2011, 2012). Here we combine these elements for the first time. This experimental design enables us to assess the extent to which Indo-Pacific coupled interactions occur when the ITF is blocked. In this case, the interbasin feedback interactions, if any, will necessarily occur through the atmospheric bridge.

We proceed by outlining the numerical model and experimental design in section 2. In section 3, the change to the mean climate with ITF closed is presented, along with the transformations of the dominant Pacific and Indian Ocean climate modes. In section 4, the importance of the atmospheric bridge is assessed with the aid of partially decoupled experiments. A discussion and summary follows in section 5.

2. The climate simulations

The simulations were conducted using version 1.2 of the Commonwealth Scientific and Industrial Research

Organization (CSIRO) Mark 3L (Mk3L) climate system model. CSIRO Mk3L is a coupled general circulation model (GCM) designed for running millennial-scale simulations (Phipps 2010; Phipps et al. 2013). The atmospheric GCM (AGCM) has a resolution of ~5.6° longitude × ~3.2° latitude, with 18 levels in the hybrid vertical coordinate. The oceanic GCM (OGCM) has double the horizontal resolution (i.e., ~2.8° longitude × ~1.6° latitude) and 21 levels in the vertical z coordinate. The AGCM and OGCM are spun up independently, after which the two are coupled with constant flux adjustments to minimize drift and maintain a realistic seasonal climatology. The version of the model used here includes the updated configuration of the Indonesian Archipelago, as employed by Santoso et al. (2012); Santoso et al. (2011) used an earlier version of the CSIRO Mk3L.

The properties of ENSO, the IOD, and the IOBM are all reasonably well simulated by the model; nevertheless, some biases exist, as already noted by Santoso et al. (2012). Here we briefly outline the principal biases. As in many Intergovernmental Panel on Climate Change (IPCC)-class climate models (e.g., Guilyardi et al. 2009), the ENSO displays a "cold tongue bias." Additionally, SST variability peaks 2–3 months earlier with weaker magnitude and a longer period than observed. The simulated IOD is stronger than in observations, consistent with the climatological biases in SST, trade winds, and rainfall over the eastern Indian Ocean. This bias renders the warm phase of the IOBM to exhibit slight cooling in the southeastern Indian Ocean (and the opposite for the cool phase), which is not apparent in observations. Furthermore, the mean ITF rate in the model is approximately 21 Sv, which is larger than the observed estimate of about 15 Sv. This is associated with the coarse model resolution partly through the joint effect of baroclinicity and relief (JEBAR; England et al. 1992; Santoso et al. 2011). Despite these shortcomings, the overall model performance is reasonable considering its resolution, which makes it ideal for centennial- to millennial-scale climate simulations.

After the initial spinup of the AGCM and OCGM, the coupled model is integrated for 400 yr, with CO_2 concentration held fixed at the preindustrial value of 280 ppm. At this point, two experiments are branched off and integrated a further 1100 yr out to year 1500. In the first, the Indonesian passage is blocked by a land bridge [as done by Santoso et al. (2011)] and, in the second, the ITF remains open. The last 200 yr of each run is used as the control experiments that we henceforth denote as CTRL$_\text{clsd}$ and CTRL$_\text{open}$, respectively. The CTRL$_\text{open}$ experiment was run primarily to compare the changes to the mean climate and modes over the Indian Ocean,

which has not been previously published. Epochs from within the CTRL$_\text{clsd}$ experiment are then used to initialize an ensemble of three 100-yr partially "decoupled" experiments, wherein air–sea interaction over the Indian and Pacific Oceans are separately suppressed. These experiments are referred to as DCPL$_\text{clsd}^\text{IO}$ for suppressed air–sea interaction over the Indian Ocean, and DCPL$_\text{clsd}^\text{PO}$ for suppressed air–sea interaction over the Pacific Ocean. The decoupling is achieved by fixing SST over the respective oceans using the climatological seasonal mean field, as done by previous studies (e.g., Baquero-Bernal et al. 2002; Behera et al. 2005; Dommenget et al. 2006; Santoso et al. 2012). The decoupled regions were bounded by 30°S and 30°N, by the coast to the east and west, and by the Indonesian archipelago. As such, the western side of the Maritime Continent warm pool is considered as part of the Indian Ocean, and the eastern side (the western Pacific warm pool) is considered as part of the Pacific Ocean. Despite this setting, the warm pool seasonal variation is retained, since the SST is fixed to the seasonally varying climatology. However, it should be noted that, in this way, our study does not explicitly consider the potential influence that variability over the Indonesia seas has on ENSO (Annamalai et al. 2010) as well as on Indian Ocean variability.

Each 100-yr partially decoupled run was initialized from the matching CTRL$_\text{clsd}$ experiment at the corresponding epoch over the 200-yr period, taken at intervals of 50 yr (i.e., initialized at year 1 for set one, year 51 for set two, and year 101 for set three). An ensemble set of three partially decoupled experiments for each case allows for the inference of statistical significance. The purpose of using 100-yr-long experiments was to ensure sufficient sampling of the low-frequency ENSO variability in each scenario, but they were limited to that length so that the decoupling did not introduce substantial model drift resulting from any potential error in air–sea heat fluxes (Fischer et al. 2005). The mean climate drift in our 100-yr-long partially decoupled experiments is small. For DCPL$_\text{clsd}^\text{IO}$, the difference in mean SST across the equatorial Pacific Ocean over 100 yr compared to CTRL$_\text{clsd}$ is less than 0.05 K. For DCPL$_\text{clsd}^\text{PO}$, the difference across the equatorial Indian Ocean is less than 0.01 K.

3. Mean climate and modes in the closed ITF control experiment

Blocking the ITF results in significant changes to the mean climate. Figure 1 shows the annual mean climate in CTRL$_\text{open}$ and CTRL$_\text{clsd}$ and the differences between the two experiments, featuring SST, surface wind stress, ocean surface currents, rainfall, and sea level pressure. Changes to the Pacific Ocean shown by Santoso et al.
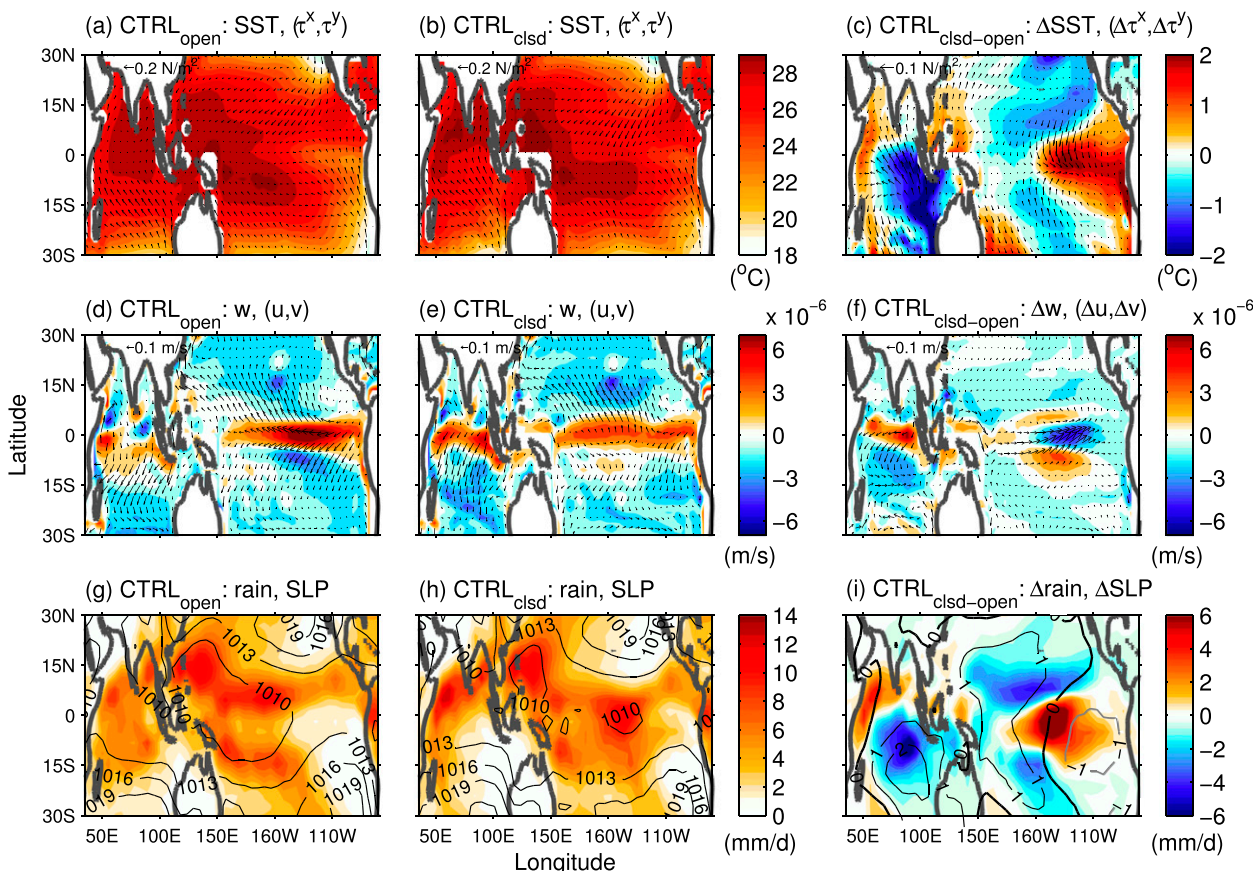
FIG. 1. Annual mean climate in CTRL_open and CTRL_clsd, along with the differences. Mean SST field is shown in color and surface wind stress with arrows for (a) CTRL_open, (b) CTRL_clsd, and (c) the differences. Mean vertical ocean velocity at 50 m is shown in color and horizontal depth-integrated ocean currents over the top 50 m are shown with arrows for (d) CTRL_open, (e) CTRL_clsd, and (f) the differences. Mean precipitation is shown in color and SLP (hPa) with contours for (g) CTRL_open, (h) CTRL_clsd, and (i) the differences.

(2011) with the earlier version of the CSIRO Mk3L model are reproduced here in Fig. 1 and briefly described for completeness. Closing the ITF dramatically changes the ocean circulation, with notable strengthening of the East Australian Current and weakening of the Agulhas Current. The equatorial Pacific thermocline slope declines, resulting in a warmer eastern Pacific that leads to higher and lower sea level pressure (SLP) in the western and eastern Pacific, respectively. This drives westerly wind anomalies and weakens the westward equatorial surface currents and upwelling. As a result, rainfall increases in the eastern Pacific and decreases in the western Pacific.

The changes to the mean climate over the Indian Ocean in the model, not discussed by Santoso et al. (2011), include cooling of the eastern Indian Ocean waters resulting from the absence of heat transported from the western Pacific via the ITF. The concurrent increase in SLP drives stronger southeasterly winds that promote equatorial upwelling and lifts the thermocline

depth, thereby further cooling the eastern Indian Ocean. The most significant change to precipitation is a large decrease over the southeastern Indian Ocean, which is consistent with the cooler SST and higher SLP in that region.

The intense cooling in the eastern Indian Ocean and lesser warming in the eastern Pacific render a slowdown of the Walker circulation across the two basins. Zonal atmospheric wind speeds over the Pacific Ocean are typically reduced by half. These changes to the mean climate and Walker circulation are illustrated as a schematic in Fig. 2 and are qualitatively consistent with previous studies that used coupled climate models to study the issue (Wajsowicz and Schneider 2001; Song et al. 2007). The other elements of Fig. 2 are discussed in section 4.

Closing the ITF significantly alters the modes of climate variability as a result of changes to the mean climate upon which they evolve (Song et al. 2007; Santoso et al. 2011). Figures 3 and 4 show the spatial patterns of
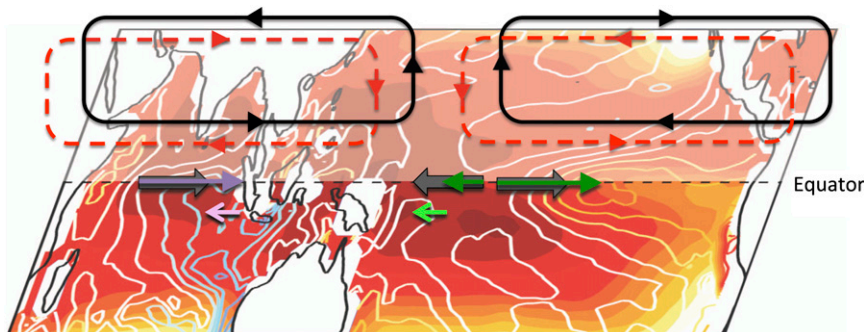
FIG. 2. Schematic of changes to the Walker circulation and surface wind stress upon closure of the ITF. In the background image, the color shading shows the mean SST field for CTRL_open (as in Fig. 1a), and the color contours represent the difference in the mean SST field between CTRL_clsd and CTRL_open (as in Fig. 1c). The black loops illustrate the typical Walker circulation in CTRL_open. When the ITF is closed, the Walker circulation weakens, as shown by the dashed red loops, designating the change. The interactions between oceanic modes in CTRL_clsd are discussed in section 4, and they are illustrated by the following: The large gray arrows along the equator denote the mean surface wind stress anomalies during the growth phase of a warm event (July–November for El Niño in the Pacific and March–June for the warm Indian Ocean phase) for CTRL_clsd. The dark green and dark purple arrows denote the same wind stress anomalies but for $DCPL_{clsd}^{IO}$ and $DCPL_{clsd}^{PO}$, respectively. The brighter green and purple arrows denote the effective influence of the opposite ocean basin. The arrows for the wind stress anomalies are reversed for La Niña and cool Indian Ocean events.

the dominant empirical orthogonal function (EOF) modes for SST. The EOF analyses were performed on the full 200-yr CTRL_open and CTRL_clsd sets for each ocean separately and bounded by 20°S–20°N. In the Indian Ocean, the IOBM (Fig. 3a) and the IOD (Fig. 3b) are the leading modes of climate variability, explaining 22% and 19% of the total variance, respectively. However, when the ITF is closed, the Indian Ocean essentially exhibits only a single mode, with the first EOF mode (EOF-1) explaining 31% of the total variance, (EOF-2 and EOF-3 correspond to only 9% and 8%, respectively). The spatial pattern exhibits a broad warming (or cooling) signature that extends westward from the eastern Indian Ocean. The pattern and temporal characteristics, as shown in section 4, are unlike that of either the IOD or the IOBM in CTRL_open. The mode, whose SSTA pattern is of uniform polarity, bears closer resemblance to an El Niño signature in the Indian Ocean given the equatorial region in CTRL_clsd is marked by strong upwelling, with trade wind and oceanic current patterns similar to those in the Pacific Ocean. For simplicity, we will refer to this mode in the CTRL_clsd experiment as the Indian Ocean mode and abbreviate it to IOM_clsd to emphasize its occurrence is unique to the closed ITF experiments.

Consistent with observations, ENSO in CTRL_open (Fig. 4a) is the leading mode, explaining 41% of the total variability. ENSO-like variability persists in CTRL_clsd (Fig. 4b) despite having its characteristics altered, in

agreement with that reported by Santoso et al. (2011) in the earlier version of the model. The core of the ENSO SSTAs is confined farther to the east in CTRL_clsd. The overall variability is reduced, primarily through the collapse of the decadal component, as the magnitude of the interannual component is largely retained (see Fig. 6f of Santoso et al. 2011), without involving any apparent change in seasonality. These alterations to ENSO are a result of the changes to the Walker circulation, which drives weaker easterly wind stresses over the equatorial Pacific (see schematic in Fig. 2).

4. Effect of suppressed air–sea interactions

To examine the response of the modes in CTRL_clsd to suppressed air–sea interactions, we constructed representative SST indices for each oceanic basin that best capture the modes of variability. An Indian Ocean central index (IOCI) was constructed by averaging SST over the region of strongest variability (5°S–5°N, 50°–100°E) for the Indian Ocean mode (IOM_clsd), as indicated in Fig. 3c. Note that the overall results do not change when the averaging box is shifted slightly to the south. To account for the eastward shift in the core region of the ENSO SSTAs in CTRL_clsd, the Niño-3 index (5°S–5°N, 150°–90°W) was adopted for this analysis, as indicated in Fig. 4b, which is captured better by the Niño-3.4 index in CTRL_open. The monthly standard deviation, power spectral densities, and autocorrelations of these two
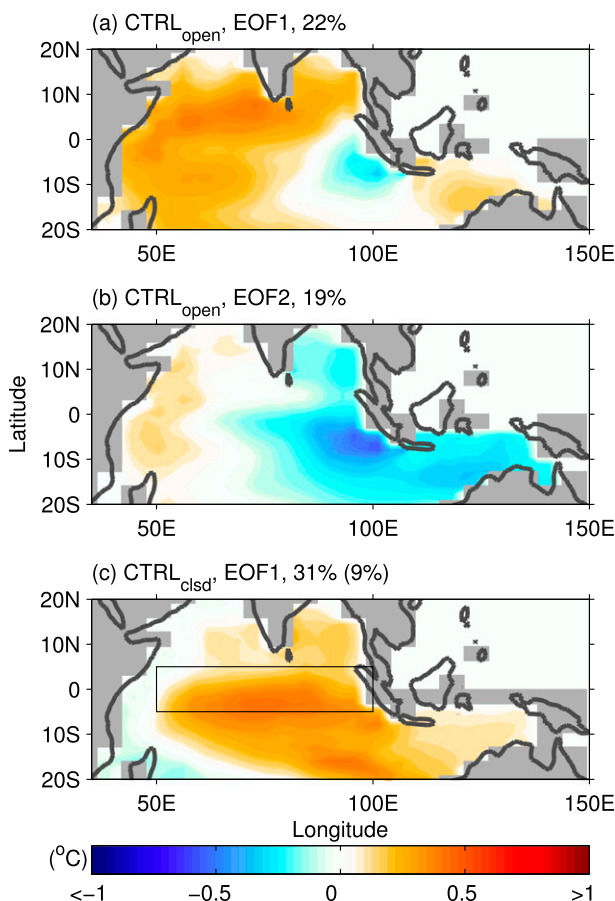
FIG. 3. The dominant EOF modes for Indian Ocean SST presented as regression maps. The two dominant modes in CTRL_open are (a) the IOBM and (b) the IOD. In CTRL_clsd, the variance is dominated by a single (c) Indian Ocean mode (IOM_clsd). The percentage of the variance explained by each mode is shown above each panel. Additionally, the variance explained by EOF-2 in CTRL_clsd is given in parentheses. The overlaid box in (c) denotes the region chosen for the Indian Ocean central index (IOCI; 5°S–5°N, 50°–100°E). The gray shading indicates the land cells in the model.

FIG. 4. The dominant EOF modes for Pacific Ocean SST presented as regression maps for (a) CTRL_open and (b) CTRL_clsd. The percentage of the variance explained by each mode is shown above each panel, with the variance explained by EOF-2 in parentheses. The overlaid box in (b) denotes the Niño-3 region (5°S–5°N, 150°–90°W), which encapsulates the core of the ENSO SSTAs in CTRL_clsd.

indices are shown in Fig. 5, for CTRL_clsd, DCPL$_{clsd}^{PO}$, and DCPL$_{clsd}^{IO}$. A notable feature of IOM_clsd is that the variability peaks during May–July (Fig. 5a), in contrast to the IOD (which peaks during August–November) and the IOBM (peaking during January–May). This seasonal phase locking in CTRL_clsd is consistent with the peak of the southeasterly winds and equatorial upwelling in austral winter (not shown).

Suppressing air–sea interactions in either oceanic basin results in amplification of the overall variability of both Niño-3 and the IOCI. This occurs without any change to the seasonality (Figs. 5a,b). The modes operate on notably different time scales: interdecadal for IOM_clsd (Fig. 5c) and interannual for ENSO (Fig. 5d).
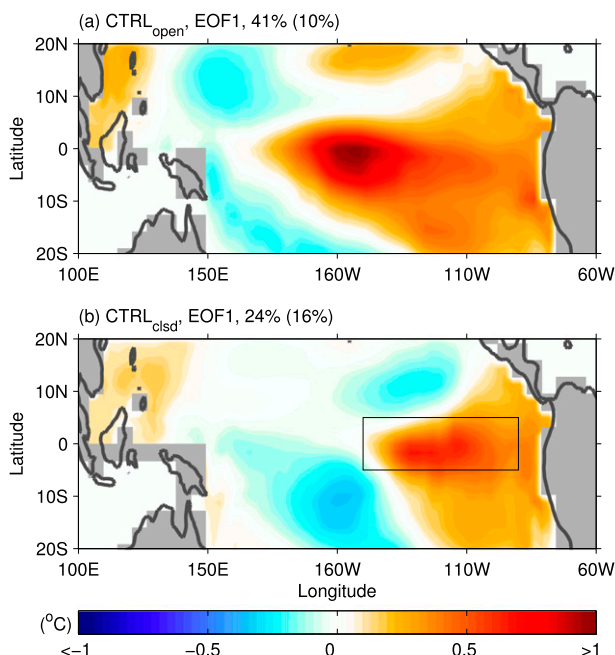
The tendency for an increase in the decorrelation time scale (Figs. 5e,f), more prominently for the IOCI, corroborates a shift in the modes toward longer periodicity.

The partially decoupled experiments show that the removal of the SST mode from one basin strengthens the other, relative to the CTRL_clsd simulations. Therefore, we conclude that damping occurs between the Pacific and Indian Ocean SST modes. Such interactions necessarily occur through the atmospheric bridge, since the ITF is blocked. Unlike the situation in CTRL_open, in which IOD and IOBM are strongly correlated with ENSO (Santoso et al. 2012), IOM_clsd tends to occur more independently from ENSO, as evidenced by a weak positive correlation between Niño-3 and the IOCI, with a maximum correlation coefficient of approximately 0.2, occurring at zero lag (not shown). Although it is statistically significant at the 95% confidence level, the weak correlation also implies that the cool phase of IOM_clsd can co-occur with an El Niño and the warm phase with a La Niña. The tendency for slightly more frequent occurrences of paired warm IOM_clsd phase with El Niño and cool IOM_clsd phase with La Niña allows the damping to occur as explained below.

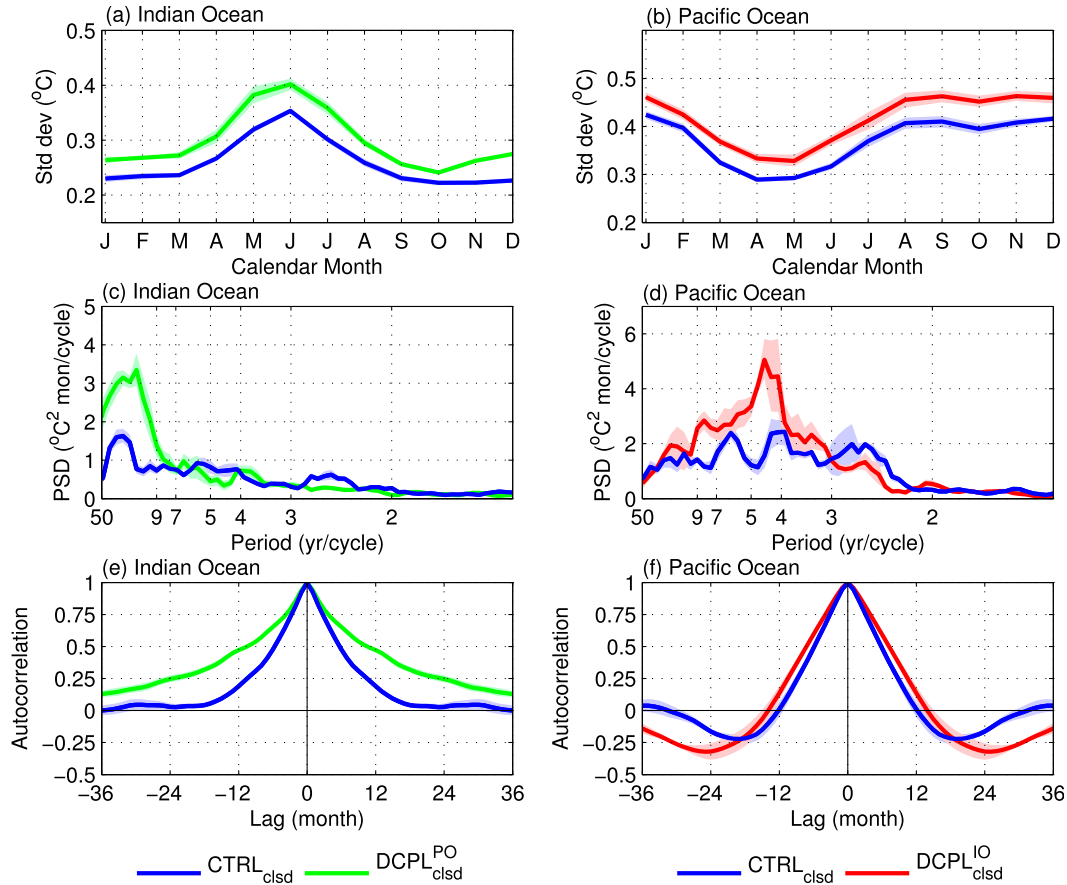The atmospheric bridge underpins the coupling between the Indian and Pacific Oceans in CTRL_clsd.

FIG. 5. Comparison of CTRL$_{\text{clsd}}$ with DCPL$_{\text{clsd}}^{\text{PO}}$ and DCPL$_{\text{clsd}}^{\text{IO}}$ for the SST index corresponding to each ocean basin. The monthly standard deviations are shown for (a) the IOCI and (b) the Niño-3 index. Note that for both cases variability is enhanced when air–sea interaction in the opposite ocean is suppressed, but the seasonality is unchanged. (c),(d) The power spectral densities for the respective indices and (e),(f) the autocorrelations. For each plot, the thick curves indicate the ensemble means. The color-shaded areas indicate the 95% confidence intervals, which were computed by dividing each 100-yr series into three 90-yr series shifted by 5 years. From the resulting nine 90-yr samples, the confidence interval was estimated based on 1000 bootstrapped means.

Figure 6a shows that suppressing air–sea coupling over the Indian Ocean results in strengthened equatorial zonal wind stress (τ^x) variability over the eastern Pacific. This is the signature of the enhanced Niño-3 variability seen in Fig. 5b. The significant weakening of τ^x variability over the Indian Ocean (between 50° and 100°E) during March–June is due to the absence of IOM$_{\text{clsd}}$ in DCPL$_{\text{clsd}}^{\text{IO}}$ (Fig. 6a). The weakened variability extends across to the western Pacific (150°E–160°W) over the latter half of the year. Thus we infer, and reinforce later, that the weakened τ^x variability over the western Pacific represents weaker τ^x anomalies in that region, which leads to enhanced τ^x anomalies over the eastern Pacific and thus permits stronger ENSO events in the absence of IOM$_{\text{clsd}}$. The damping effect of ENSO on IOM$_{\text{clsd}}$ is apparent by the strengthening of τ^x variability over the Indian Ocean in DCPL$_{\text{clsd}}^{\text{PO}}$ (Fig. 6b). The enhanced τ^x

variability manifests over the western Pacific (between 100° and 150°E) during July–October because of the removal of ENSO, and extends over the Indian Ocean (50°–100°E) during November–March.

The composite SSTA evolution of the warm and cool phases of IOM$_{\text{clsd}}$, shown in Figs. 7a and 7b, respectively, illustrates the weak correlation between the modes. In Fig. 7 and later figures, Jul(0) corresponds to July (calendar months abbreviated) in the year of the warm or cool event, and −1 or 1 in parentheses denotes the year before or after the event. In addition to the weak correlation between warm or cool events in the Indian and Pacific Oceans, there appears to be a degree of nonlinearity. Specifically, the composites show that while the warm IOM$_{\text{clsd}}$ phase coincides with some anomalous warming in the Pacific [Fig. 7a; east of 160°W during Jul(−1)–Jul(0)], the cool phase does not as frequently
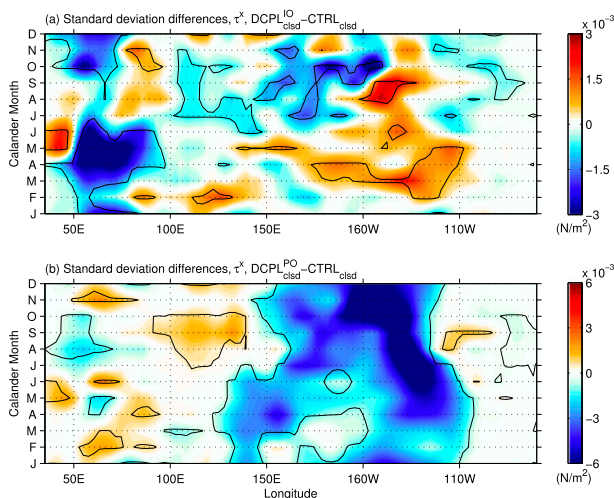
FIG. 6. Differences in monthly standard deviation of the equatorial τ^x averaged over 5°S–5°N for (a) $DCPL_{clsd}^{IO}$ minus $CTRL_{clsd}$ and (b) $DCPL_{clsd}^{PO}$ minus $CTRL_{clsd}$. The regions with different variance at the 90% confidence level under an F test are marked with solid lines.

co-occur with a La Niña (hence the weaker cool SST signature in the eastern Pacific in Fig. 7b).

The influence of IOM_{clsd} becomes apparent when the Pacific Ocean is decoupled. Figure 7c shows easterly τ^x anomalies over the western Pacific between Jul(0) and Oct(0) following the warm IOM_{clsd} phase and, conversely, westerly τ^x anomalies following the cool phase (Fig. 7d). Since this is in $CTRL_{clsd}$, it is difficult to infer the origin of these anomalies, and they may, in fact, be induced by either or both the IOM_{clsd} and ENSO modes. By decoupling the Pacific Ocean, Figs. 7e,f show that the origin of the τ^x anomalies over the western Pacific is due in large part to the Indian Ocean SSTAs, since ENSO is absent. However, the westward shift of the anomalies in $DCPL_{clsd}^{IO}$ indicates a degree of coupling to ENSO in $CTRL_{clsd}$. The τ^x anomalies correspond with a response in SLP that is anomalously low over the Indian Ocean and anomalously high over the Pacific for the warm IOM_{clsd} phase, with opposite anomalies for the cool phase. This influence of IOM_{clsd}, which is strongest during the latter half of the year (around the mature phase of ENSO), is consistent with a Kelvin wave response to zonally uniform diabatic heating over the Indian Ocean (Annamalai et al. 2005). It is further evidenced by spatially uniform rainfall changes, which can be seen by comparing Figs. 8a, b with Figs. 8c,d.

Composites of SSTAs associated with El Niño and La Niña events in Figs. 9a,b reaffirm the weak and asymmetric pairing with the warm and cool phases of IOM_{clsd} respectively. A warming signature can be seen over the

Indian Ocean during Jan(1)–Apr(1) in Fig. 9a, but a corresponding cooling signature is absent in Fig. 9b. The Indian Ocean induced easterly wind anomalies over the western Pacific enhance the wind components that are directly related to El Niño evolution (and the opposite for La Niña), which in turn exert a damping effect on ENSO variability (Santoso et al. 2012). Figures 9g,h show the differences in magnitudes of τ^x anomalies between $DCPL_{clsd}^{IO}$ (Figs. 9e,f) and $CTRL_{clsd}$ (Figs. 9c,d) for El Niño and La Niña events. For El Niño (Fig. 9g), the weakened τ^x anomalies in the western Pacific [between 150°E and 160°W during Jul(0)–Jan(1)] due to the removal of IOM_{clsd} are apparent, but for La Niña (Fig. 9h) it is less so. Conversely, the enhancement of the τ^x anomalies in the eastern Pacific (between 160° and 110°W) are more pronounced for La Niña. The weakening of the τ^x anomalies in the western Pacific is expected to be masked to some extent by the concurrent enhancement of the τ^x anomalies to the east, since the two are linked via ENSO amplitude. Nevertheless, the ENSO magnitude for both phases is consistently enhanced because of the removal of IOM_{clsd} induced wind stress anomalies in the western Pacific.

The damping effect of ENSO on IOM_{clsd} is apparent by the strengthening of the τ^x anomalies over the Indian Ocean sector in $DCPL_{clsd}^{PO}$ (Figs. 7e,f) relative to that in $CTRL_{clsd}$ (Figs. 7c,d). The strengthening occurs over the entire 24-month span that is shown, further illustrating the shift in IOM_{clsd} to longer periods in $DCPL_{clsd}^{PO}$. El Niño events induce easterly τ^x anomalies in $CTRL_{clsd}$ over the western Pacific (Fig. 9c). In the absence of IOM_{clsd}, the easterly τ^x anomalies are stronger across the Indian Ocean basin during Jan(1)–Jul(1) (Fig. 9g). These induced τ^x anomalies over the Indian Ocean are in response to the high SLP anomalies associated with anomalous cooling seen in Fig. 9a between 150°E and 140°W commencing in Jan (1), which appears to propagate eastward resulting from the more dominant ENSO thermocline feedback in $CTRL_{clsd}$ than in $CTRL_{open}$ (Santoso et al. 2011). The easterly τ^x anomalies induced by El Niño are favorable for upwelling and latent-heat-driven cooling in the Indian Ocean, and hence they exert a damping effect on the co-occurring warm phase of IOM_{clsd}. La Niña and cool IOM_{clsd} events interact similarly but with τ^x, SST, and SLP anomalies of the opposite signs to the scenario described for El Niño and warm IOM_{clsd} events. Thus, when the Pacific Ocean is decoupled, the wind stress variability associated with IOM_{clsd} is enhanced, including that over the western Pacific (Fig. 5b). This allows IOM_{clsd} to grow stronger and persist longer.

The interactive feedback between the warm IOM_{clsd} phase and El Niño in $CTRL_{clsd}$ is summarized in the
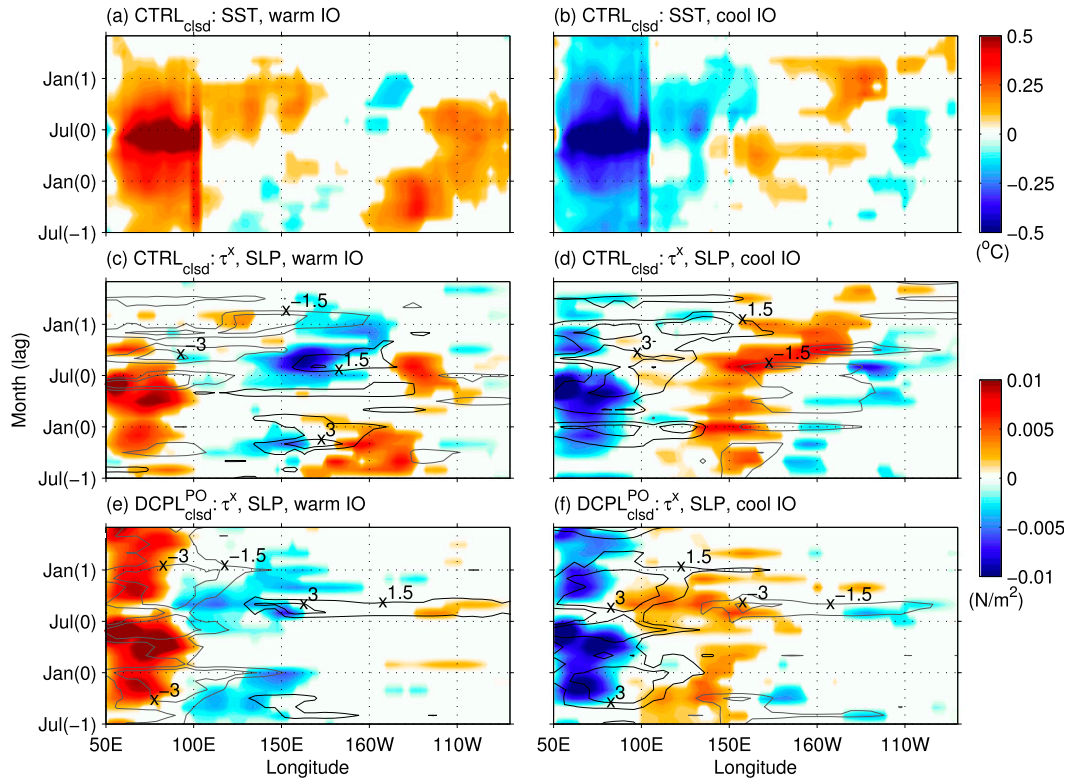
FIG. 7. Composites over 24 months of (a),(c),(e) warm and (b),(d),(f) cool Indian Ocean events for (a),(b) SST anomalies in CTRL$_{clsd}$ and for τ^x and SLP anomalies in (c),(d) CTRL$_{clsd}$ and (e),(f) DCPL$_{clsd}^{PO}$. The monthly quantities are averaged over the equatorial zone (5°S–5°N). Warm and cool events are selected when the IOCI averaged over May–July is above and below one standard deviation, respectively. Only regions that are significantly different from zero at the 90% confidence level under a t test are plotted. The SLP contours (hPa) are black for positive anomalies and gray for negative anomalies. These panels span from Jul($-$1) to Jun(1), so that the peak of the IOM$_{clsd}$ events are centered near Jul (0).

schematic of Fig. 2. In CTRL$_{clsd}$, divergent τ^x anomalies manifest over the Pacific Ocean during the growth phase of an El Niño (large gray arrows). When the Indian Ocean is decoupled, the easterly component (western Pacific) is weakened, while the westerly component (eastern Pacific) is enhanced (dark green arrows) in association with the stronger El Niño. Thus the effective influence of the warm phase of IOM$_{clsd}$ on El Niño in CTRL$_{clsd}$ is through the strengthened easterly τ^x anomalies over the western Pacific (depicted by the difference between the τ^x anomaly in CTRL$_{clsd}$ and DCPL$_{clsd}^{IO}$; bright green arrow). Over the Indian Ocean, a westerly τ^x anomaly emerges during the warm IOM$_{clsd}$ phase (large gray arrow). When the Pacific Ocean is decoupled, the τ^x anomaly is enhanced (dark purple arrow) in association with the stronger IOM$_{clsd}$. In this case, the effective influence of the developing El Niño on the warm IOM$_{clsd}$ phase is marked by the weakened westerly τ^x anomaly over the Indian Ocean (bright purple arrow denoting the difference between the τ^x anomaly in CTRL$_{clsd}$ and DCPL$_{clsd}^{PO}$).

5. Discussion and conclusions

Using a suite of coupled and partially decoupled climate model experiments, this study examined the importance of the atmospheric bridge on feedback interactions between the Pacific and Indian Oceans. To isolate the atmospheric bridge, any possible influence of the Indonesian Throughflow (ITF) was negated by introducing a land bridge across the Maritime Continent. First, it was shown that closing the ITF resulted in significant changes to modes of variability linked to changes in the mean climate. Over the Pacific, the core of the ENSO SSTAs shift eastward into the Niño-3 region, and the IOBM and IOD collapse into a single dominant Indian Ocean mode (IOM$_{clsd}$).

With the ITF closed, further experiments were conducted with air–sea interactions suppressed, firstly over the Indian Ocean, and then separately over the Pacific. Decoupling in this way eliminates any possible influence of modes of variability in that ocean basin on the other, since SSTAs in that basin are prohibited from perturbing
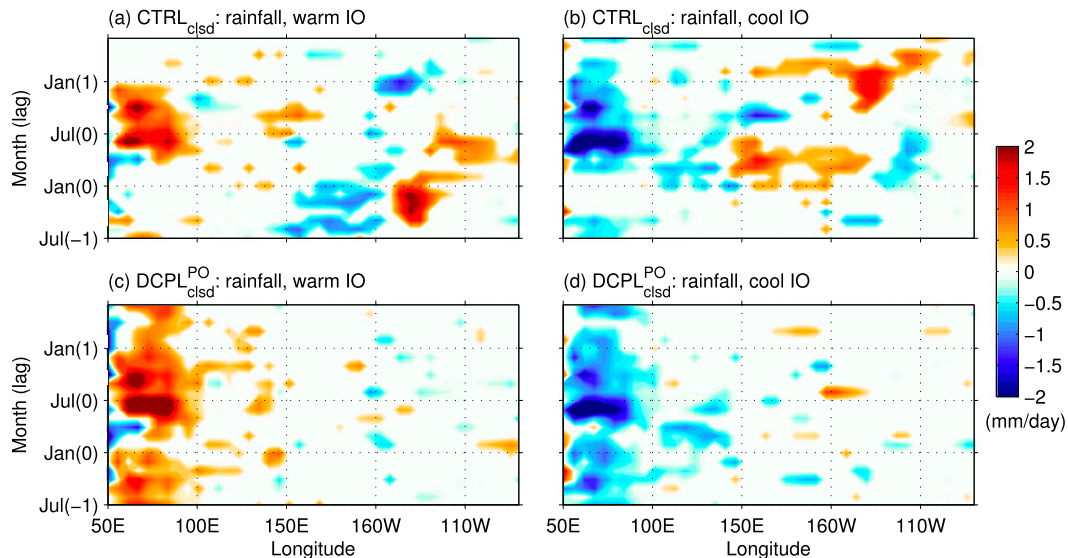
FIG. 8. As in Figs. 7c–f, but for composites of rainfall for (a),(c) warm and (b),(d) cool Indian Ocean events in (a),(b) CTRL$_{clsd}$ and (c),(d) DCPL$_{clsd}^{PO}$.

the atmosphere. It was shown that when one ocean is decoupled, SST variability over the other ocean basin is enhanced. Thus, it was inferred that the modes of variability in opposite basins act to dampen one another. This negative feedback occurs despite the fact that the occurrences of Indian Ocean SSTAs appear to be independent of the ENSO mode, and vice versa, unlike in the case when the ITF is open (Santoso et al. 2012). Nevertheless, the simulations produce a slightly stronger tendency for a warm Indian Ocean to co-occur with an El Niño. The damping effect is shown to occur through this combination. Specifically, the warm Indian Ocean SSTAs induce easterly winds over the western Pacific that exert a damping effect on the ensuing El Niño. Removing IOM$_{clsd}$ weakens these wind anomalies, and thus strengthens the ENSO mode. El Niño is also shown to induce easterly wind anomalies over the Indian Ocean that has a cooling effect through upwelling and evaporation. Such conditions are not favorable for the generation of the warm IOM$_{clsd}$ phase. This mechanism is similar but with anomalies of the opposite sign, for La Niña and the cool IOM$_{clsd}$ phase. The removal of the mode in each basin through the partial decoupling technique thus strengthens the mode in the other basin. With the ITF blocked, Indo-Pacific interactions can only occur via the atmospheric bridge.

The damping influence of the Indian Ocean on ENSO with the ITF closed is analogous to the results with ITF open. Santoso et al. (2012) found that variability of ENSO is enhanced by a similar magnitude when the Indian Ocean is decoupled. With the ITF open, they

revealed that the IOBM influences equatorial zonal wind stress τ^x over the Pacific, which acts to dampen ENSO. Specifically, the warm phase of the IOBM, which generally follows the peak of an El Niño, induces easterly τ^x anomalies over the western Pacific Ocean. This weakens the westerly τ^x anomalies that are conducive for the Bjerknes coupled air–sea feedback, so this consequently results in a weaker El Niño phase. The converse applies for the cool IOBM phase and La Niña. Thus, suppressing air–sea interactions in the Indian Ocean with the ITF open weakens τ^x variability over the western Pacific during January–April because of the removal of the IOBM, which generally coincides with the decay phase of ENSO events. We have found that a similar mechanism exists when the ITF is closed, but with an altered seasonality. The variability of the dominant climate mode in the Indian Ocean peaks during May–July with a much longer persistence, so it tends to influence ENSO during the latter half of the year, corresponding to its growth phase.

The results of Santoso et al. (2012) were consistent with Dommenget et al. (2006), who also found that Indian Ocean variability acts to dampen ENSO. Both sets of authors also agreed that the ENSO period becomes longer with the Indian Ocean decoupled. Some earlier studies had concluded that coupling ocean modes tends to increase the variability of ENSO (e.g., Barsugli and Battisti 1998; Yu et al. 2002; Wu and Kirtman 2004), but many of these were based on a single experiment with a shorter run time (on the order of 50 yr) or used an overly simplified GCM.
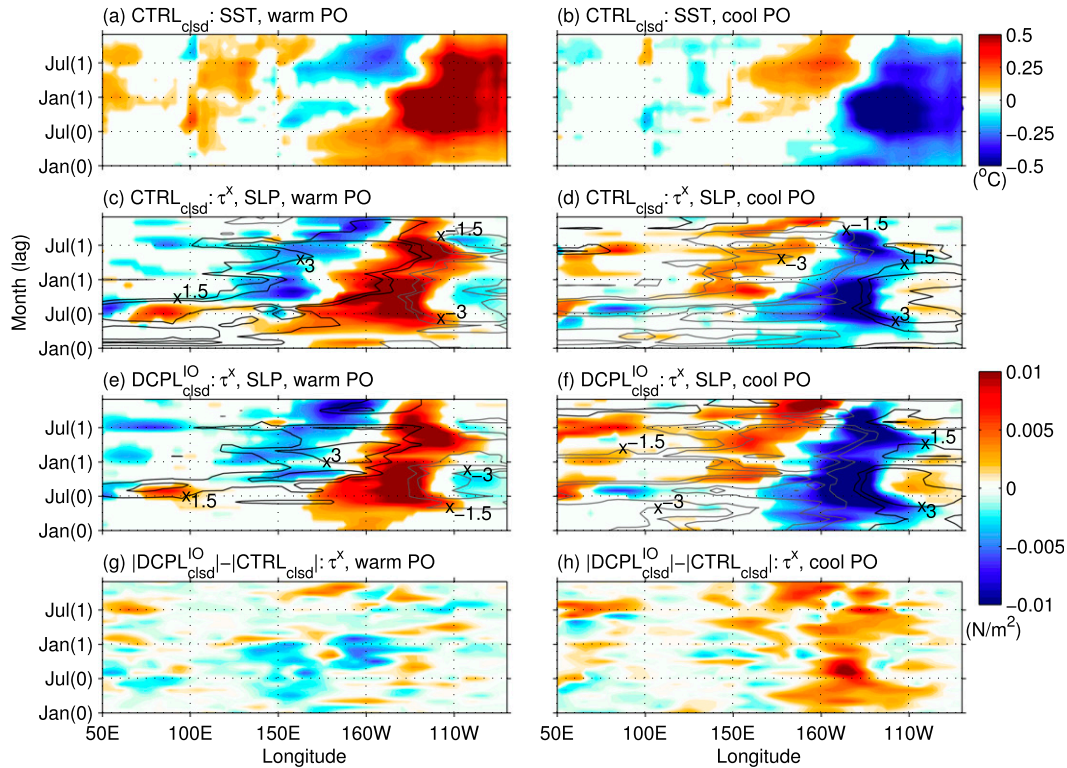
FIG. 9. Composites over 24 months of (a),(c),(e) El Niño and (b),(d),(f) La Niña events for (a),(b) SST anomalies in CTRL_clsd and for τ^x and SLP anomalies in (c),(d) CTRL_clsd, and (e),(f) DCPL_clsd^IO. (g),(h) The corresponding differences of the wind stress anomaly magnitudes |DCPL_clsd^IO| − |CTRL_clsd|. The monthly quantities are averaged over the equatorial zone (5°S–5°N). El Niño and La Niña events are selected when the Niño-3 index averaged over September–December is above and below one standard deviation, respectively. Only regions that are significantly different from zero at the 90% confidence level under a t test are plotted. The SLP contours (hPa) are black for positive anomalies and gray for negative anomalies. These panels span from Jan(0) to Dec(1), so that the peak of the ENSO events are centered near Dec(0).

In the present study, it is somewhat surprising that the atmospheric bridge mechanism remains strong despite the fact that, when the ITF is closed, the core region of the ENSO SSTAs is shifted eastward, thereby increasing the spatial separation from the Indian Ocean. The maintenance of the interbasin interactions is also reflected in the influence of the Indian Ocean mode, which is significant in CTRL_clsd. This is consistent with the uniform polarity pattern of the tropical SSTA of IOM_clsd. Such structure is more conducive for a stronger Kelvin wave response than if it were of a dipole pattern, which would otherwise generate an interference of Kelvin waves of opposite signs (Annamalai et al. 2010). We also note that the potential influence of SSTAs over the Indonesian seas on the coupling between the two basins (Annamalai et al. 2010) has not been explicitly assessed here. The present study demonstrates nonetheless that the atmospheric bridge is a robust element of the Indo-Pacific climate that would allow complex climate feedback interactions to occur even in the absence of the oceanic channel.

While the ITF has never been completely blocked in the real system [see Santoso et al. (2011) and references therein] and the behavior of the atmospheric bridge may be a function of changes in the mean climate, our results point to the possibility that modes of variability in the Indian and Pacific Oceans have been in constant interaction throughout Earth's history. This could have important implications for our understanding of Indo-Pacific climate variability in the context of past and future climates.

comments and suggestions, which helped to greatly improve the manuscript.

REFERENCES

Alexander, M. A., I. Bladé, M. Newman, J. R. Lanzante, N.-C. Lau, and J. D. Scott, 2002: The atmospheric bridge: The influence of ENSO teleconnections on air–sea interaction over the global oceans. *J. Climate,* **15,** 2205–2231, doi:10.1175/1520-0442(2002)015<2205:TABTIO>2.0.CO;2.

Annamalai, H., S. P. Xie, J. P. McCreary, and R. Murtugudde, 2005: Impact of Indian Ocean sea surface temperature on developing El Niño. *J. Climate,* **18,** 302–319, doi:10.1175/JCLI-3268.1.

——, S. Kida, and J. Hafner, 2010: Potential impact of the tropical Indian Ocean–Indonesian seas on El Niño characteristics. *J. Climate,* **23,** 3933–3952, doi:10.1175/2010JCLI3396.1.

Baquero-Bernal, A., M. Latif, and S. Legutke, 2002: On dipolelike variability of sea surface temperature in the tropical Indian Ocean. *J. Climate,* **15,** 1358–1368, doi:10.1175/1520-0442(2002)015<1358:ODVOSS>2.0.CO;2.

Barsugli, J. J., and D. S. Battisti, 1998: The basic effects of atmosphere–ocean thermal coupling on midlatitude variability. *J. Atmos. Sci.,* **55,** 477–493, doi:10.1175/1520-0469(1998)055<0477:TBEOAO>2.0.CO;2.

Behera, S. K., J.-J. Luo, S. Masson, P. Delecluse, S. Gualdi, A. Navarra, and T. Yamagata, 2005: Paramount impact of the Indian Ocean dipole on the East African short rains: A CGCM study. *J. Climate,* **18,** 4514–4531, doi:10.1175/JCLI3541.1.

——, ——, ——, S. A. Rao, H. Sakuma, and T. Yamagata, 2006: A CGCM study on the interaction between IOD and ENSO. *J. Climate,* **19,** 1688–1705, doi:10.1175/JCLI3797.1.

Cane, M. A., and P. Molnar, 2001: Closing of the Indonesian seaway as a precursor to East African aridification around 3–4 million years ago. *Nature,* **411,** 157–162, doi:10.1038/35075500.

Dommenget, D., V. Semenov, and M. Latif, 2006: Impacts of the tropical Indian and Atlantic Oceans on ENSO. *Geophys. Res. Lett.,* **33,** L11701, doi:10.1029/2006GL025871.

Du, Y., S.-P. Xie, G. Huang, and K. Hu, 2009: Role of air–sea interaction in the long persistence of El Niño–induced north Indian Ocean warming. *J. Climate,* **22,** 2023–2038, doi:10.1175/2008JCLI2590.1.

England, M. H., and F. Huang, 2005: On the interannual variability of the Indonesian throughflow and its linkage with ENSO. *J. Climate,* **18,** 1435–1444, doi:10.1175/JCLI3322.1.

——, M. Tomczak, and J. S. Godfrey, 1992: Water-mass formation and Sverdrup dynamics: A comparison between climatology and a coupled ocean–atmosphere model. *J. Mar. Syst.,* **3,** 279–306, doi:10.1016/0924-7963(92)90006-T.

Fischer, A., P. Terray, E. Guilyardi, S. Gualdi, and P. Delecluse, 2005: Two independent triggers for the Indian Ocean dipole/zonal mode in a coupled GCM. *J. Climate,* **18,** 3428–3449, doi:10.1175/JCLI3478.1.

Gordon, A. L., 2005: Oceanography of the Indonesian seas and their throughflow. *Oceanography,* **18,** 14–27, doi:10.5670/oceanog.2005.01.

Guilyardi, E., A. Wittenberg, A. Fedorov, M. Collins, C. Wang, A. Capotondi, G. J. van Oldenborgh, and T. Stockdale, 2009: Understanding El Niño in ocean–atmosphere general circulation models: Progress and challenges. *Bull. Amer. Meteor. Soc.,* **90,** 325–340, doi:10.1175/2008BAMS2387.1.

Izumo, T., and Coauthors, 2010: Influence of the Indian Ocean Dipole on the following year's El Niño. *Nat. Geosci.,* **3,** 168–172, doi:10.1038/ngeo760.

——, M. Lengaigne, J. Vialard, J.-J. Luo, T. Yamagata, and G. Madec, 2014: Influence of Indian Ocean Dipole and Pacific recharge on following year's El Niño: Interdecadal robustness. *Climate Dyn.,* **42,** 291–310, doi:10.1007/s00382-012-1628-1.

Klein, S. A., B. J. Soden, and N.-C. Lau, 1999: Remote sea surface temperature variations during ENSO: Evidence for a tropical atmospheric bridge. *J. Climate,* **12,** 917–932, doi:10.1175/1520-0442(1999)012<0917:RSSTVD>2.0.CO;2.

Kug, J.-S., and I.-S. Kang, 2006: Interactive feedback between ENSO and the Indian Ocean. *J. Climate,* **19,** 1784–1801, doi:10.1175/JCLI3660.1.

——, T. Li, S.-I. An, I.-S. Kang, J.-J. Luo, S. Masson, and T. Yamagata, 2006: Role of the ENSO–Indian Ocean coupling on ENSO variability in a coupled GCM. *Geophys. Res. Lett.,* **33,** L09710, doi:10.1029/2005GL024916.

Kuhnt, W., A. Holbourn, R. Hall, M. Zuvela, and R. Käse, 2004: Neogene history of the Indonesian Throughflow. *Continent–Ocean Interactions within East Asian Marginal Seas, Geophys. Monogr.,* Vol. 149, Amer. Geophys. Union, 299–320, doi:10.1029/149GM16.

Lau, N.-C., and M. J. Nath, 2000: Impact of ENSO on the variability of the Asian–Australian monsoons as simulated in GCM experiments. *J. Climate,* **13,** 4287–4309, doi:10.1175/1520-0442(2000)013<4287:IOEOTV>2.0.CO;2.

——, and ——, 2003: Atmosphere–ocean variations in the Indo-Pacific sector during ENSO episodes. *J. Climate,* **16,** 3–20, doi:10.1175/1520-0442(2003)016<0003:AOVITI>2.0.CO;2.

Liu, Z., and M. Alexander, 2007: Atmospheric bridge, oceanic tunnel, and global climatic teleconnections. *Rev. Geophys.,* **45,** RG2005, doi:10.1029/2005RG000172.

Luo, J.-J., R. Zhang, S. K. Behera, Y. Masumoto, F.-F. Jin, R. Lukas, and T. Yamagata, 2010: Interaction between El Niño and extreme Indian Ocean dipole. *J. Climate,* **23,** 726–742, doi:10.1175/2009JCLI3104.1.

Meyers, G., 1996: Variation of Indonesian throughflow and the El Niño–Southern Oscillation. *J. Geophys. Res.,* **101,** 12 255–12 263, doi:10.1029/95JC03729.

Phipps, S. J., 2010: The CSIRO Mk3L climate system model v1.2. Antarctic Climate and Ecosystems Cooperative Research Centre Tech. Rep., TR01-100603, 121 pp. [Available online at http://www.acecrc.org.au/access/repository/resource/017d2618-bc4e-102e-bf5a-4040d04b55e4/Climate%20model%20manual.pdf.]

——, and Coauthors, 2013: Paleoclimate data–model comparison and the role of climate forcings over the past 1500 years. *J. Climate,* **26,** 6915–6936, doi:10.1175/JCLI-D-12-00108.1.

Potemra, J. T., 1999: Seasonal variations of upper ocean transport from the Pacific to the Indian Ocean via Indonesian straits. *J. Phys. Oceanogr.,* **29,** 2930–2944, doi:10.1175/1520-0485(1999)029<2930:SVOUOT>2.0.CO;2.

——, and N. Schneider, 2007a: Influence of low-frequency Indonesian Throughflow transport on temperatures in the Indian Ocean in a coupled model. *J. Climate,* **20,** 1339–1352, doi:10.1175/JCLI4146.1.

——, and ——, 2007b: Interannual variations of the Indonesian throughflow. *J. Geophys. Res.,* **112,** C05035, doi:10.1029/2006JC003808.

Saji, N. H., B. N. Goswami, P. N. Vinayachandran, and T. Yamagata, 1999: A dipole mode in the tropical Indian Ocean. *Nature,* **401,** 360–363.

Santoso, A., W. Cai, M. H. England, and S. J. Phipps, 2011: The role of the Indonesian Throughflow on ENSO dynamics in a coupled climate model. *J. Climate,* **24,** 585–601, doi:10.1175/2010JCLI3745.1.

——, M. H. England, and W. Cai, 2012: Impact of Indo-Pacific feedback interactions on ENSO dynamics diagnosed using ensemble climate simulations. *J. Climate,* **25,** 7743–7763, doi:10.1175/JCLI-D-11-00287.1.

Schneider, N., 1998: The Indonesian Throughflow and the global climate system. *J. Climate,* **11,** 676–689, doi:10.1175/1520-0442(1998)011<0676:TITATG>2.0.CO;2.

Song, Q., G. A. Vecchi, and A. J. Rosati, 2007: The role of the Indonesian Throughflow in the Indo-Pacific climate variability in the GFDL coupled climate model. *J. Climate,* **20,** 2434–2451, doi:10.1175/JCLI4133.1.

Sprintall, J., and A. Révelard, 2014: The Indonesian throughflow response to Indo-Pacific climate variability. *J. Geophys. Res. Oceans,* **119,** 1161–1175, doi:10.1002/2013JC009533.

——, S. Wijffels, R. Molcard, and I. Jaya, 2009: Direct estimates of the Indonesian Throughflow entering the Indian Ocean: 2004–2006. *J. Geophys. Res.,* **114,** C07001, doi:10.1029/2008JC005257.

van Sebille, E., J. Sprintall, F. U. Schwarzkopf, A. S. Gupta, A. Santoso, M. H. England, A. Biastoch, and C. W. Böning, 2014: Pacific-to-Indian Ocean connectivity: Tasman leakage, Indonesian Throughflow, and the role of ENSO. *J. Geophys. Res. Oceans,* **119,** 1365–1382, doi:10.1002/2013JC009525.

Vranes, K., A. L. Gordon, and A. Ffield, 2002: The heat transport of the Indonesian Throughflow and implications for the Indian Ocean heat budget. *Deep-Sea Res. II,* **49,** 1391–1410, doi:10.1016/S0967-0645(01)00150-3.

Wajsowicz, R. C., and E. K. Schneider, 2001: The Indonesian Throughflow's effect on global climate determined from the COLA Coupled Climate System. *J. Climate,* **14,** 3029–3042, doi:10.1175/1520-0442(2001)014<3029:TITSEO>2.0.CO;2.

Wang, B., R. Wu, and R. Lukas, 1999: Roles of the western North Pacific wind variation in thermocline adjustment and ENSO phase transition. *J. Meteor. Soc. Japan,* **77,** 1–16.

Wijffels, S. E., G. Meyers, and J. S. Godfrey, 2008: A 20-yr average of the Indonesian Throughflow: Regional currents and the interbasin exchange. *J. Phys. Oceanogr.,* **38,** 1965–1978, doi:10.1175/2008JPO3987.1.

Wu, R., and B. P. Kirtman, 2004: Understanding the impacts of the Indian Ocean on ENSO variability in a coupled GCM. *J. Climate,* **17,** 4019–4031, doi:10.1175/1520-0442(2004)017<4019:UTIOTI>2.0.CO;2.

Yu, J.-Y., C. R. Mechoso, J. C. McWilliams, and A. Arakawa, 2002: Impacts of the Indian Ocean on the ENSO cycle. *Geophys. Res. Lett.,* **29,** 1204, doi:10.1029/2001GL014098.

Yuan, D., and Coauthors, 2011: Forcing of the Indian Ocean dipole on the interannual variations of the tropical Pacific Ocean: Roles of the Indonesian Throughflow. *J. Climate,* **24,** 3593–3608, doi:10.1175/2011JCLI3649.1.

——, H. Zhou, and X. Zhao, 2013: Interannual climate variability over the tropical Pacific Ocean induced by the Indian Ocean dipole through the Indonesian Throughflow. *J. Climate,* **26,** 2845–2861, doi:10.1175/JCLI-D-12-00117.1.